POLITECNICO DI TORINO
Repository ISTITUZIONALE

Combining Mathematical Modeling and Thermal Infrared Data in the Freezing of Pharmaceutical Liquid
Formulations

(Article begins on next page)

26 April 2024

Article

Combining Mathematical Modeling and Thermal Infrared Data in the Freezing of Pharmaceutical Liquid Formulations

Maitê Harguindeguy, Lorenzo Stratta, Davide Fissore, and Roberto Pisano*

Read Online

ACCESS | Metrics & More | Article Recommendations

ABSTRACT: Infrared-based (IR) thermal imaging data was combined here with mathematical modeling to describe the freezing process of a pharmaceutical formulation being lyophilized using two different loading configurations; (i) vials in direct contact with the shelf and (ii) vials suspended over it. In all the experiments, the nucleation event was triggered at a specific time instant using the vacuum induced surface freezing (VISF) method. The IR thermal data was given as input to three different mathematical models for freezing and used to estimate the resulting cake's pore size (d_p) distribution. The resulting d_p values were then compared to experimental data obtained through SEM images coupled with an image segmentation tool. The supersaturation model showed the best agreement between the estimated d_p and experimental values, while minor discrepancies were shown by the other two models. Nonetheless, the outcomes of these last two models, given as inputs to a mathematical model for the primary drying phase, resulted in satisfactory predictions of the product temperature at the moving front, the product resistance to vapor flow, and the primary drying end point. It follows that the combination of the IR thermocamera and freezing modeling is a promising tool for the in-line monitoring and optimization of a freeze-drying cycle.
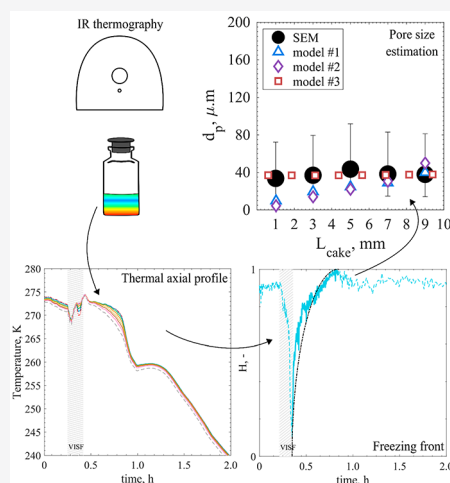
1. INTRODUCTION

Recently, the pharmaceutical industry faced a substantial renovation, as the production of drugs moved from small, chemically synthesized molecules to biopharmaceuticals. However, these products are often unstable in liquid solutions for prolonged periods. At the same time, they tend to lose their drug activity if exposed to the high temperatures required in conventional drying. In this context, freeze-drying has attracted great interest, as it is a drying technique involving low temperatures. Freeze-drying is composed of three main phases: freezing, primary drying, and secondary drying. During freezing, the solution containing the active pharmaceutical ingredient combined with other excipients is frozen and cooled to temperatures between 220 and 235 K. Then, during primary drying, the chamber pressure is reduced, reaching values of a few Pascals (Pa), while heat is continuously supplied to promote sublimation of the frozen solvent. Once sublimation is completed, further heat is provided during secondary drying, allowing the desorption of the unfrozen water from the remaining solid matrix.

For many years, the efforts of the scientific community focused mainly on the optimization of primary drying, as it is the longest step of the process. Freezing, however, recently obtained its due attention. Many papers were published on the subject, unveiling its effects on the product structure[1−3] and biological residual activity.[4−6] The dimension and intercon-nectivity of the pores in the dried cakes, which are the footprints of the sublimated ice crystals, are thought to be directly correlated with the freezing protocol used, particularly the nucleation temperature, the cooling rate, and the thermal gradients within product being frozen.

The cake structure strongly influences the maximum temperature reached by the product during primary drying and, therefore, its duration. Pores with large diameters and high interconnectivity offer relatively low resistance to mass transport (R_p) in the dried layer, resulting in high values of water vapor flux at low temperatures. This condition allows the implementation of more aggressive process conditions and, therefore, reduces the primary drying time. Hence, the knowledge of the structure of the dried product is crucial for the definition of the optimal cycle for a specific product, and the possibility to have this knowledge in-line, instead of after an explorative experimental campaign, would give an incredible advantage in terms of material use and time saved.

During the past few years, numerous mathematical models were proposed describing the evolution of the ice crystals in pharmaceutical solutions during freezing. Some of these models are empirical[7−9] or mechanistic[10] or even based on the Universal QuasiChemical (UNIQUAC) model.[11] However, even though carefully validated with extensive experimental campaigns, all these models, to some extent, still rely on heat and mass transfer models within the liquid being frozen.

Commonly, the temperature measurements are done using thermocouples in the research and development scale or temperature remote interrogation systems (TEMPRIS) in an industrial scale. These sensors cannot give temperature distributions, only punctual estimations usually obtained placing the probe at the bottom of the product. Moreover, they are invasive probes; thus, they strongly interfere with the measured system, i.e., increasing the nucleation temperature when used to monitor the freezing process. Additionally, the acquired data must be extrapolated to the neighboring vials, assuming similarities in the conditions, which do not always correspond to reality. To overcome this problem, it is possible to use different technologies.[12] Freezing was experimentally studied using simple image analysis to obtain the freezing progression in a solution.[13,14] In recent years, many papers have been produced to validate and study the application of infrared (IR) imaging as a noninvasive method to obtain in-line temperature measurements during freeze-drying.[15−17] This technology is up-and-coming not only because it does not interfere with the process itself but also because it can provide temperature distributions among vials both in the freezing and in the drying stages. The ability to obtain a full thermogram of the products temperature profile provides an almost complete knowledge of the system without introducing additional heat transfer models. However, a few open points remain to be analyzed. In particular, no one has applied the IR imaging methodology yet to the various forms of controlled nucleation techniques. In the pharmaceutical industry, freezing is often performed by applying predetermined temperature ramps on the thermally controlled shelves of the freeze-dryer. However, due to the high stochasticity of the nucleation phenomena, the nucleation temperature can vary in a wide range of temperatures in a single batch. Considering the already mentioned strong effects of nucleation on the whole process, this stochasticity is one of the leading causes of intrabatch variability and on the product's quality.

For this reason, many methods to control nucleation have been proposed. The most relevant are the ice-fog technique,[18] the pressurization−depressurization technique,[19] the induction of nucleation by application of ultrasounds[20] or electric fields,[21] and the vacuum induced surface freezing (VISF) technique.[22−27] In the present paper, the focus will be given to VISF, the sole technique applicable without hardware upgrades on the current freeze-dryers. As the technique's name suggests, VISF is performed by lowering the chamber pressure when all the vials reach the desired nucleation temperature. The reduced pressure promotes evaporation at the surface of the solution, which, in turn, dramatically cools the upper solution layer due to the latent heat of evaporation. If the pressure is lowered fast enough, the temperature at the solution's surface drops to such a degree that spontaneous nucleation is locally induced, triggering nucleation in the rest of the solution. Once nucleation is induced in the whole batch, atmospheric pressure is restored by a stream of nitrogen, and then, freezing can be completed.

The VISF technique has been studied and described in detail in the past.[22−24,28,29] Nonetheless, in the present work, IR-based experimental data will be used to predict the cake structure using three different freezing models: the one presented by Nakagawa et al.,[9] Arsiccio et al.,[10,27,30] and Colucci et al.[11] The results will then be compared and discussed to obtain a better insight into which conditions the models work best and in which they fail.

In detail, this work combines different freezing models and IR thermography for the prediction of the pore size distribution of lyophilized samples frozen by VISF. The temperature acquisition will be made in-line by thermal imaging, obtaining the entire axial temperature profile within the vial and, thus, allowing for a detailed prediction of the pore size distribution. Moreover, the range of applicability of the three models was tested upon two loading configurations: the conventional loading configuration where vials are in direct contact with the shelf and the case in which vials are suspended over the shelf. In the first configuration, heat is transferred from the shelf to the vials, or vice versa, mainly through direct contact between the vial bottom and the shelf and through conduction in the gas trapped in the concavity at the vial's bottom. In contrast, when vials are suspended, heat is transferred mainly due to natural convection and radiation. This difference in the heat transfer mechanism challenges the usual assumption of negligible radial and azimuthal thermal gradients. Without this assumption, the in-line application of freezing models to experimental IR data is limited.

The predicted cake structures will then be validated by comparing the pore sizes obtained through the models with the experimental ones obtained through SEM analyses. Additionally, primary drying temperature profiles and time will be simulated based on the estimated pore sizes and compared to the experimental data.

2. EXPERIMENTAL SECTION

2.1. Experimental Apparatus and Formulations. All the experiments were conducted in a laboratory-scale freeze-dryer LyoBeta 25 (Telstar, Terrassa, Spain). The freeze-dryer is composed of a 0.2 m^3 vacuum-sealed chamber with four 0.16 m^2 temperature-controlled shelves. A butterfly valve connects the main chamber to the 0.12 m^3 condenser. The freeze-dryer is equipped with a capacitance manometer (Baratron type 626A, MKS Instruments, USA, accuracy: ±0.25% of reading) and a thermal conductivity gauge (Pirani type PSG-101-S, Inficon, Switzerland, accuracy: ±15% of reading). The ratio of the two signals (Pi/Ba) depends on the chamber atmosphere composition and was used to detect the end point of primary drying, when all the water is evacuated from the chamber and substituted with nitrogen, thus changing the value of this ratio.[31,32]

Three formulations were used as model products: 10% w/w dextran 40 kDa (PanReac AppliChem, Chicago, USA), 5% w/w sucrose, and mannitol formulations (Sigma-Aldrich, Milano, Italy). The solutions were prepared with water for injection (WFI) (Fresenius Kabi, Verona, Italy) and filtered with 0.22 μm PVDF sterile filters (Merck Millipore, Cork, Ireland). Tubing vials (4R type, Nuova Ompi, Piombino Dese, Italy) were filled with 1 mL of solution and prestoppered with silicon igloo stoppers (West Pharmaceutical Service, Milano, Italy). The resulting cake depth was 10 mm.

Temperature profiles were monitored using an IR sensor system (IMC Service S.r.l., Italy). This system includes a built-in thermal camera (FLIR Systems model A35; FLIR Systems Inc., Wilsonville, OR, USA), a WiFi antenna for wireless data transfer, and a processing board. The vials were positioned at an approximate distance of 25 cm, the focal distance of the IR sensor system. The glass used in the manufacturing of the vials is almost entirely opaque to IR radiations, whereas the IR sensor only detects the temperature of the vials' glass surface and not the temperature of the product. To account for this discrepancy, Van Bockstal et al.[33] proposed a 1-D model to calculate the temperature gradients forming along the radial direction within the glass vial wall. However, it was also demonstrated that these gradients are generally smaller than 0.2 K,[17] at least in the range of conditions used in this work, which could be considered negligible given the accuracy of the IR sensor (± 1 K). Thus, the IR reading will be attributed directly to the product throughout the paper for simplicity.

2.2. Freeze-Drying Process Protocols. A total of 10 vials were used in each experiment. Two different loading configurations were used to test different heat transfer mechanisms, as described in Figure 1. The choice of using
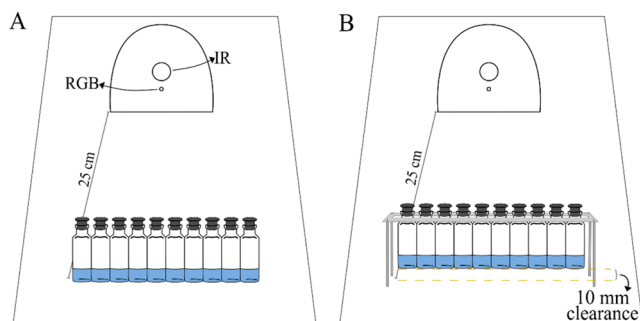

Figure 1. Experimental setups used (not to scale). (A) ON-shelf setup, vials in direct contact with the shelf. (B) OFF-shelf setup, vials suspended by plexiglass tracks and screws.

two loading configurations aims at enlarging the set of experimental data, further testing the application of thermal imaging to the freezing of pharmaceutical solutions, and checking the limits of applicability of the various mathematical models under different conditions. In the ON-shelf configuration, the vials were placed in direct contact with the shelf. In this way, the heat was mainly transferred to the product by conduction between the temperature-controlled shelf and the vials' bottom. In the OFF-shelf configuration, the vials were suspended with two Plexiglas tracks held by screws, as presented by Capozzi et al.,[34] having a 10 mm $\pm$ 1 mm clearance. In this way, the heat was mainly transferred by natural convection and radiation from the temperature-controlled shelves and the surrounding walls.

Nucleation was induced in all the experiments using the VISF technique after an equilibration time of ~1 h at the selected nucleation temperature, T_n. The chamber pressure was reduced as fast as possible to approximately 1 to 2 mbar and held until nucleation was visually detected in all the vials. After nucleation occurred, atmospheric pressure was restored using a stream of dry nitrogen. Two values of T_n were used, $T_{n,1} = 271$ K and $T_{n,2} = 263$ K, in order to distinguish the effects of different nucleation temperatures on the average ice crystal size. The first one, 271 K, was close to the solution equilibrium

temperature, and the second one, 263 K, was close to the temperature at which spontaneous nucleation was observed in preliminary experiments (263 K).

The shelf temperatures, $T_{sh,1}$ and $T_{sh,2}$, were explicitly set, depending on the vial loading setup, in order to equilibrate vials at, respectively, $T_{n,1}$ and $T_{n,2}$. More specifically, $T_{sh,1} = 268$ K and $T_{sh,2} = 258$ K for the ON-shelf configuration, and $T_{sh,1} = 262$ K and $T_{sh,2} = 248$ K for OFF-shelf vials. After nucleation, the temperature of the shelf was maintained at the holding temperature T_h for ~1 h to ensure complete freezing. $T_{h,1}$ and $T_{h,2}$ were, respectively, 258 K for ON-shelf vials and 248 K for OFF-shelf ones, which corresponded to $T_{sh,2}$. All the conditions used in this work are summarized in Table 1. Then, the shelf temperature was lowered to 223 K at 0.5 K/min and kept at that temperature for ~2 h.

Table 1. Test Names According to the Solution, T_n, T_{sh}, T_h, and Setup Used

test name	solution	T_n	T_{sh}	T_h	setup
1-D	10% dextran	271	268	258	
1-S	5% sucrose				
1-M	5% mannitol				ON-shelf
2-D	10% dextran	263	258	258	
2-S	5% sucrose				
2-M	5% mannitol				
3-D	10% dextran	271	262	248	
3-S	5% sucrose				
3-M	5% mannitol				OFF-shelf
4-D	10% dextran	263	248	248	
4-S	5% sucrose				
4-M	5% mannitol				

Primary and secondary drying were performed under the same conditions for all the experiments, ensuring that the product temperature always remained below its critical value to avoid any shrinkage/collapse of the dried cake. These critical values are 241.15 K for 5% sucrose, 263.15 K for 10% dextran, and 258.15 K for 5% mannitol.[35] The pressure in the chamber was set to 5 Pa. Then, the shelf temperature was increased from 223 to 253 K as fast as possible and maintained at 253 K for 15 h to ensure complete primary drying. This specific primary drying temperature was the highest allowing the product temperature to remain below its critical value in the whole set of experiments. After this holding time, the shelf temperature was raised from 253 to 293 K in 4 h and then maintained for 2 h at 293 K to complete secondary drying. At the end of the process, ambient pressure was restored by the bleeding of nitrogen. Then, the vials were stoppered, sealed with aluminum caps, and stored in a freezer at 253 K for further evaluation.

2.3. Product Morphology Characterization. The pore size was determined using a Desktop SEM Phenom XL (Phenom-World B.V., Netherlands) at an accelerating voltage of 15 kV. The samples were extracted from the vials and cut vertically to obtain a thin slice corresponding to the axial section. The slice was then fixed on an aluminum circular stub and metallized with platinum using a sputter coater (Balzer AG, type 120B, Balzers, Liechtenstein). The samples were extracted directly in the laboratory. However, they were analyzed right after the extraction in order to minimize the possibility of water uptake. SEM pictures of the product were taken along five levels on the vertical axis within three different

radial positions to fully represent the porous cake structure with magnifications from 210× to 270×. The SEM images obtained were 1088 × 1024 pixels. These images were segmented using image processing techniques[36] like the *Canny algorithm*[37] for edge detection coupled with Multivariate Image Analysis[38] as previously described[39] to extract the pore size distribution.

2.4. Freezing Models. Various models were proposed in the literature to describe the solidification process of a pharmaceutical solution. The first two models presented here are based on a freezing front that advances as freezing progresses. These models may be adapted to a three-dimensional space by assuming a unidirectional freezing front evolution for each examined fraction of the evaluated system. However, a direct application of these models is possible when the freezing front evolution can be considered unidirectional, and the experimental IR-based data may be used to verify this. Unfortunately, this was the case only for vials in direct contact with the shelf, under the current IR sensor settings. In this case, the heat is exchanged mainly between the bottom of the vials and the shelves and in the gap between them, while convection and radiation to the vial sidewalls can be considered negligible. The temperature at the bottom of the vial, T_{bottom}, is therefore the lowest during the freezing step. Thus, the first two models will only be applied to the ON-shelf experiments for a direct application of the proposed models using experimental IR data. The third ice crystal prediction model presented ahead does not rely on the unidirectional heat-exchange assumption and is based only on the product's state specifically on its temperature. Thus, only the product temperature is needed for calculations, and it can be directly applied to both ON- and OFF-shelf experiments using experimental IR-based data.

Model #1. The model presented by Nakagawa and Hottot (2007)[40] to predict ice crystal size for solutions in vials will be called throughout this paper model #1 and estimates the average ice crystal diameter, d_p, for each cake section i as

$$d_p = \alpha \times \nu_i^{\lambda 1} \times \theta_i^{\lambda 2} \tag{1}$$

Here, ν_i is the freezing front rate $[\text{m·s}^{-1}]$, i.e., how fast the freezing front advances. The parameter θ_i is the temperature gradient in the frozen layer $[\text{K·m}^{-1}]$, i.e., corresponds to the temperature difference between the temperature at the bottom of the vial, T_{bottom}, and the temperature at the freezing front, T_{ff}, relative to the frozen layer thickness in the case of unidirectional freezing. In previous applications of this model, $\lambda 1 = \lambda 2 = 0.5$ were used, while α was experimentally fitted to the resulting pore sizes and changed according to the solution and freezing protocol used.[40−42] $\alpha = 4.59 \ \mu\text{m s}^{-0.5} \text{K}^{-0.5}$ was used for a 5% sucrose solution, while $\alpha = 1.7 \ \mu\text{m s}^{-0.5} \text{K}^{-0.5}$ was used for a 5% mannitol one.[17,40,41] For 5% dextran, the α used was the same as the one for sucrose. In the present study, the same α values were used for sucrose and mannitol, and a value of 2 $\mu\text{m s}^{-0.5} \text{K}^{-0.5}$ was chosen for 10% dextran, based on the experimental results. The 10% dextran solution presented overall smaller pore sizes than 5% sucrose resembling more the 5% mannitol cake. Using the 5% sucrose α, the resulting d_p predictions were larger than the experimental results. Thus, since this is an experimentally fitting parameter that is formulation-specific, using the 2 $\mu\text{m s}^{-0.5} \text{K}^{-0.5}$ α value resulted in better estimations for this solution.

Model #2. Model #2 is the mechanistic model proposed by Arsiccio et al. (2017).[10] This model assumes that all the crystals are cylinders with a diameter (d_p) and gives more physical grounding to its parameters than the previously proposed models for freezing in vials. The average ice crystal diameter, d_p, for each cake section i is calculated as

$$d_p = \frac{4\varepsilon\gamma b\nu_i}{(\varepsilon\rho_{ice}\nu_i\Delta H_f - k_{frozen}\theta_i)\theta_i^{2/3}} \tag{2}$$

Here, ε is the nondimensional porosity of the dried product, which can be approximated assuming that all water in the solution is removed, and only the solids constitute the dried cake. The k_{frozen} used in this study was 2.55 W/m·K, corresponding to the ice conductivity at 238 K, ΔH_f, the latent heat of fusion for water, was 33.5 kJ·kg^{-1}, and ρ_{ice} was 918 kg·m^{-3}.[43] The parameter γb is fitted experimentally, according to the solution and freezing protocol similarly to the α value in model #1. Thus, the γb values used were 23000 J·K$^{(\frac{2}{3})}$·m$^{(\frac{-8}{3})}$, 7000 J·K$^{(\frac{2}{3})}$·m$^{(\frac{-8}{3})}$, and 8000 J·K$^{(\frac{2}{3})}$·m$^{(\frac{-8}{3})}$ for 5% sucrose, 5% mannitol, and 10% dextran, respectively.[10] The first two were found in the literature,[10,17] while the value was stipulated for dextran based on the experimental results, following the same logic as the α value in model #1.

Model #3. Model #3, the *Supersaturation model*, is based on the hypothesis that the nucleation and crystallization processes are driven by the supersaturation of the system. This way, model #3 estimates the crystal sizes for a system based on its temperature and solution characteristics. The solutes and solution activity coefficients are described from the free Gibbs energy perspective, similar to the approach presented by Colucci et al.[11]

First, the initial nucleation rate, B_0, is calculated to determine the initial number of ice nuclei formed during the nucleation event $[\text{m}^{-3}\text{·s}^{-1}]$.

$$B_0 = k_n(T_f - T_n)^n \tag{3}$$

B_0 depends on the supercooling degree $(T_f - T_n)$, i.e., the difference between the equilibrium freezing temperature of a solution, T_f and the actual nucleation temperature, T_n. The kinetic parameters k_n and n are based on the stochastic nature of freezing and are explained in more detail elsewhere.[11] They can be calculated by experimental fit, and in this study, using controlled nucleation, the values used were $k_n = 1.3 \times 10^{10}$ m^{-1}·s^{-1} and $n = 1.7$. These values were stipulated and verified based on experimental data and modeling. The used model only included one nucleation event; hence, the final number of crystals is determined by B_0. Different k_n and n values were tested to yield roughly the same ice crystal size number per volume as observed in SEM images of the resulting cake. Then, the best k_n and n were further evaluated by checking the induction time distribution they would yield, as better described in Colucci et al. (2020).[11] The resulting induction times using these k_n and n values were within the experimentally observed ones of ~100 s using VISF[39] and, thus, were deemed adequate.

The growth rate is assumed proportional to the surface area of the single crystals and the supersaturation (σ) of the system as the driving force. Assuming cylindrical crystals and neglecting the surface of the top and bottom of the cylinders, the crystal growth rate (G, ms^{-1}) was calculated as
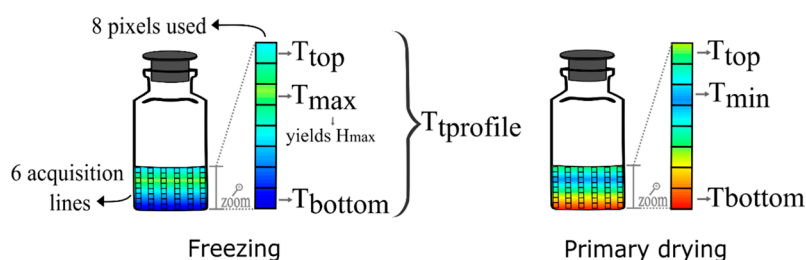
Figure 2. Scheme to portray the IR thermal data acquisition lines and pixel resolution used. Additionally, it is shown how data acquisition was made using the vertical IR-based vial temperature profile and the relevant variable during freezing and primary drying.

$$G(D_p, t) = k_g \sigma^g 2\pi \Delta z D_{P_{t-1}} = G'(t) D_{P_{t-1}} \tag{4}$$

$$D_p(t) = D_{P_{t-1}} \exp\left\{ \int_{t_0}^{t_{end}} G'(t) \, \mathrm{d}t \right\} \tag{5}$$

The supersaturation (σ) of the system is given by the difference between the activity coefficients of the frozen and liquid fractions based on the UNIQUAC model.[44] The ice activity is defined by its temperature and molar fraction.[45] The liquid activity depends on the temperature and the solute nature and concentration. It was calculated as proposed by Catté et al.[44] for sucrose, by Norrish[46] for mannitol, and by De Vito et al.[47] for dextran.

The kinetic parameters k_g and g are highly dependent on the time step used for the integration interval. In the literature, using time steps from 0.02 to 0.5 s in a completely simulated environment, i.e., simulating all heat exchange and resulting nucleation and crystal growth,[11] $k_g 2\pi \Delta z$ was set as 10 s^{-1} (meaning $k_g = 1592$ m$^{-1}\cdot$ s^{-1}), while g was set as 1. In this study, using only experimental IR-based temperature data, $k_g 2\pi \Delta z = 1$ s^{-1} and $g = 1$ were used with an integration time step of 0.01 s. The integration interval $t_0 - t_{end}$ corresponds to the time intercurring from nucleation to the end of freezing. The end of freezing was based on the eutectic point, T_{eu}, for the 5% mannitol solutions (251.7 K) and on the glass transition temperature, T'_g, for the sucrose (240 K) and dextran solutions (264 K).[35]

The parameter $2\pi \Delta z$ is a dimensional term assuming that the ice crystals are approximately cylindrical. D_p gives the evolution of the crystal size distribution for the evaluated section in the system, the monitored section that provides the thermal readings. The first D_p at t_0 was calculated using a one-dimensional population balance model (PBM) assuming it follows a beta distribution with $\beta_1 = 1.2$ and $\beta_1 = 15$,[11] having characteristic lengths ranging from 0 to 0.5 μm. This is the driving factor that will determine the crystal size distribution throughout the freezing simulation. $D_{P_{t-1}}$ is the previous D_p state at time $t - 1$. The D_p at the end of freezing (t_{end}) is the resulting predicted ice crystal size distribution for the evaluated section.

The volume of water that forms the ice nuclei is determined based on the supersaturation of the system, and then, from the initial state (nucleation), crystal growth is calculated using eqs 4 and 5. D_p yields the average ice crystal sizes (d_p) for each section through the ratio between the first- and the zeroth-order moments of the pore size distribution as described by Colucci et al.[11]

2.5. IR Data Acquisition and Processing. Figure 2 shows an example of the temperature profile within the product being frozen and, then, dried. The maximum and

minimum temperatures and their positions could be detected by monitoring the axial temperature profile through IR images. By averaging the temperatures of the six acquisition vertical lines within each vial, it is possible to obtain the average vial temperature. By averaging the mean temperatures of all the vials of the batch, one obtains the average batch temperature. Since freezing is an exothermic phenomenon, by tracking T_{max} and H_{max}, the freezing front velocity, ν_i, and the temperature gradient in the frozen layer, θ_i, can be inferred. Analogously, since sublimation is an endothermic process, T_{min} gives the sublimation interface temperature, T_i, during primary drying. Based on the assumption $T_{min} \approx T_i$, T_{min} profiles were confronted with the simulated T_i profiles to further validate model #1 and model #2, as explained in section 2.6.

Eight pixels were used for each data acquisition line in order to cover the entire product depth. The whole axial temperature profile ($T_{profile}$) was obtained by averaging each of these 8 pixels from the six vertical acquisition lines. The $T_{profile}$ is the only experimental information needed for model #3. With this axial profile, the nucleation and crystal growth rate can be calculated for each pixel, thus, for each cake fraction. Furthermore, the crystal growth is calculated for each cake layer using its thermal profile during freezing, defined by the eight acquisition pixels. The temperature profiles presented in this paper were smoothed with a Savitzky−Golay filter to reduce data noise.

2.6. Primary Drying Simulation. In addition to confronting the estimated ice crystal sizes to the effective pore sizes through SEM images, models #1 and #2 were further validated for the case of ON-shelf batch configuration. For these models, primary drying was simulated in silico to obtain T_i and the R_p which were then confronted to the experimentally measured T_{min} and the R_p calculated based on the T_{min}. Since all tests had the same T_{shelf} and chamber pressure conditions, these were the ones also used in the simulations.

The calculation to simulate the primary drying was based on a steady-state heat balance for the frozen product. To this end, the overall heat exchange coefficient, K_v, was determined nongravimetrically, using the IR-based end-time determination method as proposed by Harguindeguy and Fissore (2020).[16] In this method, because sublimation is an endothermic process, the sublimation interface temperature (T_i) was monitored during primary drying by tracking the minimum axial temperature, T_{min}. Because IR is noninvasive and it does not interfere with the sample,[15] the temperature rise when sublimation is completed served as a consistent primary drying end-time determination method. By assuming that all water sublimated in the time interval is defined by the T_{min} tracking method, the K_v could be determined nongravimetrically.[16] The
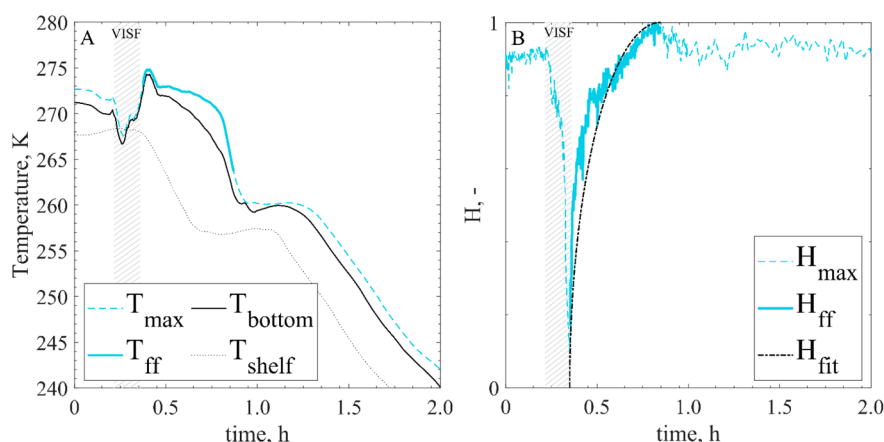
Figure 3. Maximum temperature profiles during freezing for dextran 10%, test 1-D. (A) Temperature gradient between the bottom (T_{bottom}) and the maximum axial temperature (T_{max}) measured. (B) Position of the maximum axial temperature (H_{max}) and fit used (H_{fit}) for the models along the vial's adimensional axis where 0 is the bottom and 1 is the top. In graphs (A) and (B), T_{max} and H_{max} are plotted with a continuous light blue line during the accounted freezing interval, representing the freezing front temperature (T_{ff}) and position (H_{ff}), respectively.

average value of K_v for the six ON-shelf batches was 33.0 ± 4.4 W·m^{-2}·K^{-1}.

The sublimation interface temperature, T_i, was calculated recursively together with R_p using well-known one-dimensional heat exchange models and suitable assumptions. For the sake of brevity, they are not described here, as they were described in detail by Harguindeguy and Fissore 2021.[16] The only addition done in the present work was a different equation for the R_p calculation. Commonly, R_p is calculated from experimental data as a function of product temperature and chamber pressure. However, in the present work, the aim is to evaluate the validity of the estimated resulting pore sizes by different freezing models. Thus, R_p was calculated using the ice crystal sizes estimated by models #1 and #2 to the R_p as follows[48]

$$R_p = \frac{R_g T_i^{0.5}}{K \varepsilon M_w \frac{d_p}{2\tau}} L_{dried}$$

(6)

where R_g is the gas constant (8315 J·K^{-1}·mol^{-1}), L_{dried} is the thickness of the dried layer, K is a constant parameter equal to 22.9 m·s^{-1} K$^{0.517}$, ε is the nondimensional porosity of the dried product as in model #2, M_w is the molecular weight of water (18 g mol^{-1}), and τ is the tortuosity of the cake ($\tau = 1$ was used). This R_p is important to determine not only the T_i but also the sublimation flux needed to estimate process duration in terms of the remaining frozen layer (L_{frozen}).

2.7. Statistical Analysis. Pore size distribution in the freeze-dried product was previously found to follow a beta distribution with $\beta_1 = 1.2$ and $\beta_1 = 15$.[39] Thus, the pore size distribution data spread is expressed in terms of the first and third quartiles. All calculations were done in MATLAB (version 9.7.0 R1019b).

3. RESULTS AND DISCUSSION

3.1. Infrared-Based Temperature Profiles and Freezing Front Evolution. In practical terms, water in solution never freezes *completely*. After nucleation, pure ice is formed, and the solution cryo-concentrates. Once the system reaches a characteristic concentration, dependent on the excipient, the cryo-concentrated solution remains in a supercooled single-phase state, which could be amorphous or crystalline. Water

molecules get trapped into the excipient solidified matrix and are unable to diffuse and crystallize further.[45,49] For this reason, freezing is usually regarded as *complete* when the solution reaches the glass transition temperature, T_g', for amorphous solutions or the eutectic point, T_{eu}, for crystalline ones.

However, it was observed in the present work that the temperature gradients inside the vials almost disappeared after the product reached nearly 260 K, which is, for sucrose and mannitol, several degrees higher than their T_g' and T_{eu}. An example of this can be seen in Figure 3 (graph A) where the gradient expressively reduces by 0.9 h of the freezing step. The profile trends and behavior observed for dextran were virtually the same as those observed for 5% mannitol and 5% sucrose. Thus, their graphical results are not presented, although they are discussed in the manuscript.

Thermodynamically speaking, at temperatures close to 260 K, most of the water, that is supposed to freeze, has already changed phase; only a small fraction of the total would further crystallize. The latent heat of solidification release became less pronounced, and the product temperature tended to be more homogeneous. Under these considerations and by tracking H_{max} and T_{max}, it is therefore possible to detect a moving freezing front only during the first 20 min after nucleation for the ON-shelf vials. Moreover, the choice of this time scale agrees with what was previously reported for the same cake depth.[34] Hence, the time required to reach a temperature of 260 K is the freezing interval that will be considered to obtain the freezing front rate (ν_i) and the temperature gradient within the frozen layer (θ_i) based on the T_{max} and H_{max} profiles.

Model #1 and Model #2. Figure 3 (graph A) shows the evolution of T_{bottom}, T_{max}, T_{shelf} and T_{ff} during freezing. After nucleation, T_{max}, which corresponds to the T_{ff} and H_{max} are marked more expressively with a thicker continuous line to stress the freezing interval considered for the application of models #1 and #2. T_{bottom} and T_{ff}, during this interval, are used in the models to calculate θ_i. Models #1 and #2 can be applied to the axial, radial, azimuthal freezing, and the combination of these three. However, an accurate description of the temperature distribution inside the freezing solution is necessary in order to obtain ν_i and θ_i. While trivial for the ON-shelf vials, in which the freezing front advances vertically while radial and azimuthal temperature gradients are negligible, the situation is
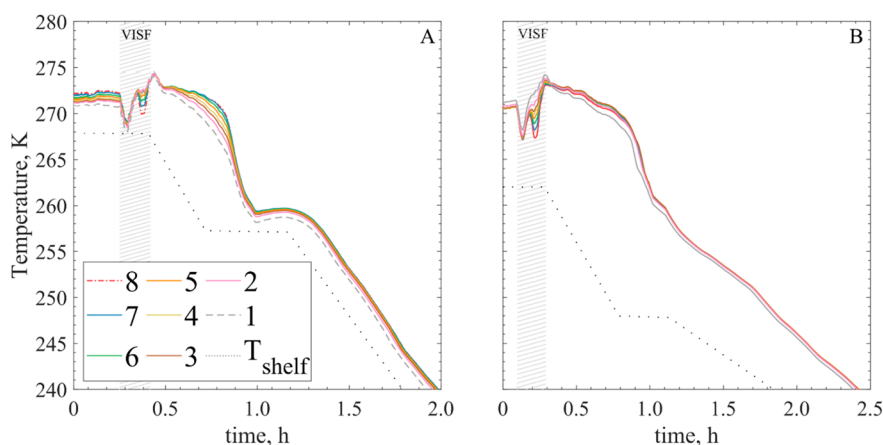
Figure 4. Axial temperature profile (A) for 1-D (ON-shelf) and (B) 3-D (OFF-shelf). Lines 1 to 8 represent the pixels for data extraction from bottom to top, respectively.

more challenging for the OFF-shelf vials. Due to the different heat transfer mechanisms involved, i.e., natural convection and thermal radiation, the radial temperature gradients are not negligible anymore. The freezing front moves in two directions, vertical and radial, and the IR camera, which records the temperature of the product in contact with the vial wall solely, fails in acquiring the required information. When these models were developed, the temperature was monitored with thermocouples, which provides a single-punctual temperature measurement. The problem was overcome by applying accurate heat-transfer models forecasting the temperature profile, knowing the temperature of the solution at the bottom of the vials. Solving the aforementioned heat-transfer models would require an accurate description of the individual heat transfer mechanisms involved in the process, which is not trivial. In this case, a single global heat transfer coefficient is not sufficient. Thus, to allow a direct in-line application using IR-based data, models #1 and #2 were applied only to the ON-shelf vials, and the OFF-shelf ones were studied with model #3, which do not necessitate such information.

As freezing advances, the temperature difference $T_{ff} - T_{bottom}$ increases. When the freezing front reached the top layers of the product, almost 90% of the water had already frozen from thermodynamic calculations, and little to no latent heat could be further released. Consequently, after the first ~20 min, T_{max} decreased rapidly, eventually reaching the T_{bottom} and thus defining the end of freezing. The H_{max} profile was assumed to represent the freezing front profile. In Figure 3 (graph B), H_{max} is plotted together with the fit that was used in the d_p calculations to have a continuous progression of the H_{max} profile. As can be seen in Figure 3, H_{fit} did not perfectly follow the evolution of H_{max}. Right after nucleation the freezing front moved particularly, and unexpectedly, fast toward the top of the solution, and the fit did not manage to follow such a trend. As will be discussed subsequently, this deviation could be the reason for inconsistencies between the models and the experimental results. However, the utilization of a fitting curve was made necessary by the irregular, oscillating behavior of the H_{max} profile, which could not thus be used *as was* in the models.

Model #3. As previously explained, model #3 is not dependent on the gradients but rather on the temperature at the points of interest. The thermal history of each pixel was therefore used to estimate the ice crystal growth for the

corresponding cake layer. Thus, the cake was divided into eight levels corresponding to the eight pixels of the vertical acquisition lines. For each level, the corresponding pixels of the six acquisition lines were averaged to obtain a mean temperature and then used to calculate the crystal size distribution for each cake layer. Figure 4 shows an example of the axial temperature profile obtained for both the ON-shelf and OFF-shelf vials.

As shown in Figure 4, in the OFF-shelf vials, the temperature profiles of the eight product layers were almost identical, in contrast to the ON-shelf vials in which the layers were subjected to greater differences. Based on model #3, this observation means that the resulting cake structures should be more homogeneous for the OFF-shelf vials than for the ON-shelf ones. Indeed, it is consistent with what is expected since the heat transfer for the OFF-shelf vials was less sharp than for the ON-shelf vials, which exchanged heat directly in contact with the cooling shelf.

3.2. Model Validation through SEM Images. Figure 5 shows the predicted pore sizes based on the ice crystal growth models confronted with the experimental SEM results for the 10% dextran solution. The results for the 5% mannitol and 5% sucrose solutions were very similar and presented the same trends observed for the 10% dextran solutions.

As shown in Figure 5, models #1 and #2 could predict the average pore size with some accuracy. However, graph A shows that toward the edges of the cake (top and bottom), the prediction of the pore size became less accurate. This deviation may be attributed to the differences observed between the experimental IR-based freezing front profile and the extrapolated ones used in the models, see Figure 3 (graph B). The simulated freezing front progression used for the application of the models showed a more regular progression of the frozen layer, almost following a linear profile.[9,10,27] The IR-based experimental data, in turn, presented a sharp advancement of the freezing front at the beginning of freezing and, then, a deceleration approaching the cake top surface. The profile of the freezing front directly influences the ν_i, and in the experimental data, the values of ν_i were incredibly high at the beginning and, then, particularly low toward the end. This result could be explained by the variation in the thermal conductivities of the materials involved as the freezing went ahead. Ice has a higher k_v (2.22 W·m⁻¹ K⁻¹) than water (0.6 W·m⁻¹ K⁻¹) at 293 K; however, slightly melted snow has an
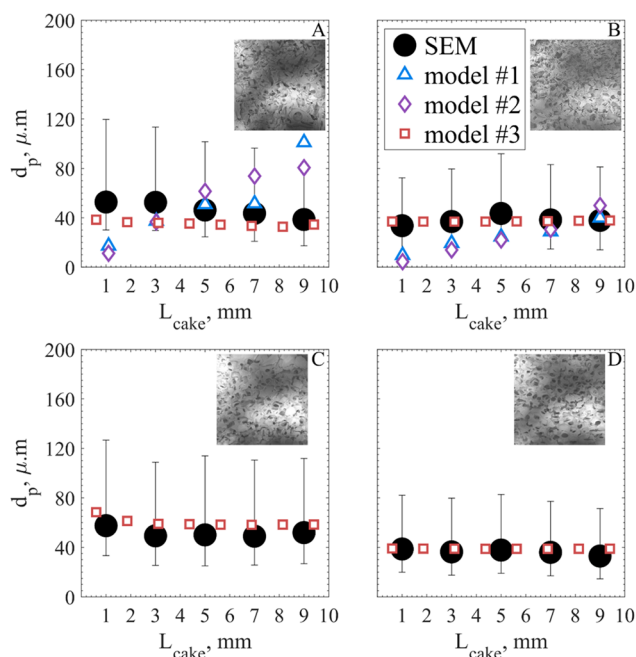
Figure 5. Average pore size as predicted by model #1, model #2, and model #3 plotted together with the pore sizes from the SEM images. The results refer to 10% dextran as processed in (A) test 1-D, (B) test 2-D, (C) test 3-D, and (D) test 4-D. An SEM image extracted from the middle of the cake for each test is presented in each graph as representative of the cake for that test.

even lower k_v (0.28 W·m^{-1} K^{-1}) than water. The characteristics of slightly melted snow are surely closer to the ones of a mushy ice−water region. This increase in the resistance to heat transfer by the growing mushy layer may be the reason for this deceleration on the presumed freezing front, based on the T_{max} profile. Given these considerations, using experimental data and the models #1 and #2 *as is*, the predictions seemed unreliable for the bottom and top of the cake.

The results obtained for model #3 were much more accurate throughout the whole cake depth. This model presented a superior affinity with the experimental application of the temperature profiles by IR. The main limitation of model #3 in practical applications is its ability to only give a punctual product morphology prediction based on the temperature measurement. Nonetheless, because the experimental IR camera monitoring data provided the whole cake axial temperature profile, this model described the cake, using each of the eight temperature profile measurements taken for the vertical axial thermal data.

The calculations and tests done through this model showed that the nucleation conditions had the most pronounced impact on the resulting crystal size. After nucleation, the temperature profile played more of a kinetic role, driving the freezing duration rather than influencing the resulting crystal size. This estimated effect could be different if a secondary nucleation term was inserted in the model. Secondary nucleation involves the production of new crystals in a solution containing pre-existing crystals where the newly formed ice crystals themselves serve as an initiation surface nucleation.[50] The kinetics of secondary nucleation is complicated by the variation in the number of crystals and the supersaturation.[51] This insertion is a modification that could be examined in future studies.

3.3. Model Validation through Primary Drying Simulation (Models #1 and #2).

Further validations were done for the one-dimensional models besides confronting the simulated pore size distributions with those observed through SEM images. This analysis was then used to predict the product behavior during primary drying, which was then compared with the experimental data in terms of product temperature and progression of the ice sublimation. To provide an example, Figure 5 compares the model estimations of the sublimating ice front, T_i, and the thickness of the frozen layer, L_{frozen}, with their experimental observations. T_{min} is assumed to be representative of T_i, since sublimation is an endothermic phenomenon. Hence, T_{min} was monitored using IR thermography. The evolution of the calculated remaining L_{frozen} was used to estimate the end of primary drying and, thus, is compared to the experimentally obtained Pi/Ba signal.

Because of the recursive method used, the simulated thermal profiles presented a discrepancy compared to the experimental data within the first few minutes of drying. After this initial phase, the simulated data well described the experimental profiles in the case of 10% dextran, see Figure 6. This
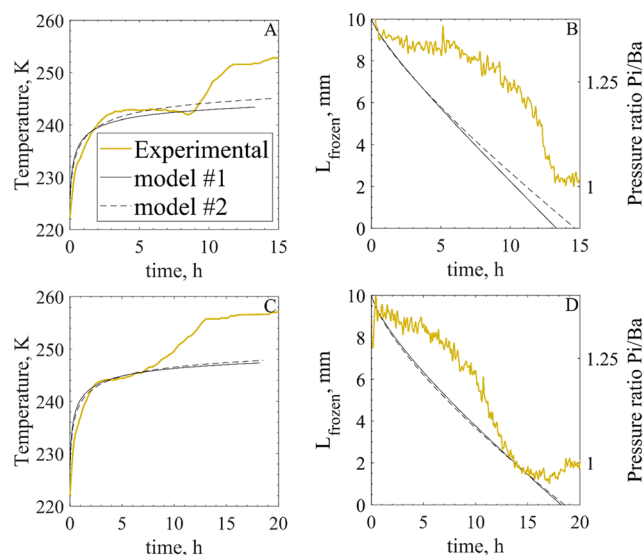

Figure 6. Comparison between model predictions by model #1 and model #2 and experimental data during primary drying. Data refer to the freeze-drying of 10% dextran processed using the ON-shelf configuration and the process conditions described in (top graphs) test 1-D and (bottom graphs) test 2-D.

agreement was also observed for 5% sucrose and 5% mannitol (data not shown). Regarding the experimental data shown in Figure 6, the thermal IR profiles showed a rising trend after ~10 h of primary drying which indicates that sublimation was over. However, the Pi/Ba signal showed that the offset of primary drying was after ~14 h, while simulations predicted the primary drying end point at ~14 h and ~18 h for the 1-D and 2-D batches, respectively. It follows that the mathematical model overestimated the drying time dependence on the pore size with respect to what was experimentally observed.

Still, the results do help in estimating the product temperature profile during drying and the process duration with adequate accuracy. Thus, it is possible to successfully apply these models with IR-based data to simulate freezing and drying and choose the best drying conditions to avoid collapse or damage to the heat-sensitive active compounds.

4. CONCLUSIONS

The IR-imaging allowed the in-line application of different freezing models to predict the resulting pore cake structure. The experimentally observed freezing front in terms of the H_{max} presented an initial steep trend at the beginning of freezing (cake bottom) and a slowdown toward the end (cake top). This profile change affected the value of the term ν_i in models #1 and #2 which, in turn, translated to less accurate d_p estimations for the bottom and top of the cakes. Thus, the resulting estimated pores based on the IR data did not always conform to the observed pore sizes using SEM. Future modifications to the existing models can be proposed to better predict the pore sizes based on the experimental IR data taking this unpredicted profile of the freezing front rate into consideration.

On the other hand, the supersaturation model was very stable and often resulted in better estimations of the resulting pore sizes. This model seemed to be highly influenced by the nucleation temperature alone, having very little influence from the temperature profiles after freezing. Since the nucleation temperature was controlled through VISF in all tests, predicting a remarkably homogeneous cake structure is not surprising. Moreover, being that the experimental data is in good agreement with the simulated ones, it is possible to advance the hypothesis that the ice crystal size distribution is driven mainly by the nucleation temperature, regardless of the thermal profile after nucleation, under the studied conditions. This hypothesis does not apply to other particular conditions, as it is well-known, for example, that annealing influences ice morphology. However, in conditions similar to those tested in this work, i.e., involving induced nucleation, postnucleation holding steps, relatively slow cooling ramps, and no annealing steps, the good agreement between simulations and experimental results confirms its validity.

The joint application of the IR-imaging and suitable models was demonstrated to be a viable tool for the in-line monitoring of freeze-drying and the prediction of the product structure. With such information, it can become possible to estimate the primary drying dynamics accurately and optimize the freeze-drying cycles without extensive experimental campaigns, changing the process conditions to fit in the best way the characteristics of the products as they are produced.

■ AUTHOR INFORMATION

Corresponding Author

Roberto Pisano − *Molecular Engineering Laboratory, Department of Applied Science and Technology, Politecnico di Torino, IT-10129 Torino, Italy;* ⊙ orcid.org/0000-0001-6990-3126; Email: roberto.pisano@polito.it

Authors

Maitê Harguindeguy − *Department of Applied Science and Technology, Politecnico di Torino, IT-10129 Torino, Italy*

Lorenzo Stratta − *Molecular Engineering Laboratory, Department of Applied Science and Technology, Politecnico di Torino, IT-10129 Torino, Italy;* ⊙ orcid.org/0000-0002-3909-285X

Davide Fissore − *Department of Applied Science and Technology, Politecnico di Torino, IT-10129 Torino, Italy*

Complete contact information is available at:
https://pubs.acs.org/10.1021/acs.iecr.1c04595

■ ABBREVIATIONS

IR, infrared; VISF, vacuum induced surface freezing; SEM, scanning electron microscope; PBM, population balance model

Nomenclature

B_0 volumetric nucleation rate, $m^{-3} \cdot s^{-1}$

dp pore size, m

D_p pore size distribution, m

H_{max} adimensional axial position of T_{max}, -

g crystal growth kinetic parameter, -

G crystal growth rate, $m \cdot s^{-1}$

K constant parameter, $m \cdot s^{-1}\ K^{0.5}$

k_{frozen} ice conductivity, $W/m \cdot K$

k_g crystal growth kinetic parameter, $m^{-1} \cdot s^{-1}$

k_n nucleation kinetic parameter, $m^{-1} \cdot s^{-1}$

L_{dried} dried cake thickness, m

L_{frozen} frozen cake thickness, m

M_w molecular weight of water, $g\ mol^{-1}$

n nucleation kinetic parameter, -

R_g gas constant, $J \cdot K^{-1} \cdot mol^{-1}$

R_p cake resistance to vapor flow, $m \cdot s^{-1}$

t_0 time zero of freezing, s

T_{bottom} product temperature at the vial bottom, K

t_{end} final freezing time, s

T_{eu} eutectic point, K

T_f equilibrium freezing temperature of a solution, K

T_{ff} temperature at the freezing front, K

T'_g glass transition temperature, K

T_i temperature at the sublimation interface, K

T_{max} maximum axial temperature, K

T_n nucleation temperature, K

$T_{profile}$ product axial temperature profile, K

T_{shelf} shelf temperature, K

Greek letters

α model #1 constant, $m \cdot s^{-0.5} \cdot K^{-0.5}$

β_1 beta distribution shape parameter, -

β_2 beta distribution shape parameter, -

γb model #2 constant, $J \cdot K^{(\frac{2}{3})} \cdot m^{(\frac{-8}{3})}$

ΔH_f latent heat of fusion for water, $J \cdot kg^{-1}$

Δz ice crystal length, m

ε nondimensional porosity of the dried product, -

θ_i temperature gradient of the frozen layer, $K \cdot m^{-1}$

$\lambda 1, \lambda 2$ model #1 constant, -

ν_i freezing front rate, $m \cdot s^{-1}$

ρ_{ice} ice density, $kg \cdot m^{-3}$

σ supersaturation of the system, -

τ tortuosity of the cake, -

■ REFERENCES

(1) Hottot, A.; Vessot, S.; Andrieu, J. Freeze Drying of Pharmaceuticals in Vials: Influence of Freezing Protocol and Sample Configuration on Ice Morphology and Freeze-Dried Cake Texture. *Chem. Eng. Process. Process Intensif.* **2007**, *46* (7), 666−674.

(2) Searles, J. A.; Carpenter, J. F.; Randolph, T. W. The Ice Nucleation Temperature Determines the Primary Drying Rate of Lyophilization for Samples Frozen on a Temperature-controlled Shelf. *J. Pharm. Sci.* **2001**, *90* (7), 860−871.

(3) Kasper, J. C.; Friess, W. The Freezing Step in Lyophilization: Physico-Chemical Fundamentals, Freezing Methods and Consequences on Process Performance and Quality Attributes of Biopharmaceuticals. *Eur. J. Pharm. Biopharm.* **2011**, *78* (2), 248−263.

(4) Arsiccio, A.; Pisano, R. The Ice-Water Interface and Protein Stability: A Review. *J. Pharm. Sci.* **2020**, *109* (7), 2116−2130.

(5) Arsiccio, A.; McCarty, J.; Pisano, R.; Shea, J. E. Heightened Cold-Denaturation of Proteins at the Ice-Water Interface. *J. Am. Chem. Soc.* **2020**, *142* (12), 5722.

(6) Fang, R.; Tanaka, K.; Mudhivarthi, V.; Bogner, R. H.; Pikal, M. J. Effect of Controlled Ice Nucleation on Stability of Lactate Dehydrogenase During Freeze-Drying. *J. Pharm. Sci.* **2018**, *107* (3), 824−830.

(7) Bomben, L.; King, C. J. Heat and Mass Transport in the Freezing of Apple Tissue. *Int. J. Food Sci. Technol.* **1982**, *17* (5), 615−632.

(8) Kochs, M.; Körber, C.; Nunner, B.; Heschel, I. The Influence of the Freezing Process on Vapour Transport during Sublimation in Vacuum-Freeze-Drying. *Int. J. Heat Mass Transfer* **1991**, *34* (9), 2395−2408.

(9) Nakagawa, K.; Hottot, A.; Vessot, S.; Andrieu, J. Modeling of Freezing Step during Freeze-Drying of Drugs in Vials. *AIChE J.* **2007**, *53* (5), 1362−1372.

(10) Arsiccio, A.; Barresi, A. A.; Pisano, R. Prediction of Ice Crystal Size Distribution after Freezing of Pharmaceutical Solutions. *Cryst. Growth Des.* **2017**, *17* (9), 4573−4581.

(11) Colucci, D.; Fissore, D.; Barresi, A. A.; Braatz, R. D. A New Mathematical Model for Monitoring the Temporal Evolution of the Ice Crystal Size Distribution during Freezing in Pharmaceutical Solutions. *Eur. J. Pharm. Biopharm.* **2020**, *148*, 148−159.

(12) Moino, C.; Bourlés, E.; Pisano, R.; Scutellà, B. In-Line Monitoring of the Freeze-Drying Process by Means of Heat Flux Sensors. *Ind. Eng. Chem. Res.* **2021**, *60* (26), 9637−9645.

(13) Vuist, J. E.; Linssen, R.; Boom, R. M.; Schutyser, M. A. I. Modelling Ice Growth and Inclusion Behaviour of Sucrose and Proteins during Progressive Freeze Concentration. *J. Food Eng.* **2021**, *303*, 110592.

(14) Becheleni, E. M. A.; Rodriguez-Pascual, M.; Lewis, A. E.; Rocha, S. D. F. Influence of Phenol on the Crystallization Kinetics and Quality of Ice and Sodium Sulfate Decahydrate during Eutectic Freeze Crystallization. *Ind. Eng. Chem. Res.* **2017**, *56* (41), 11926−11935.

(15) Harguindeguy, M.; Fissore, D. Temperature/End Point Monitoring and Modelling of a Batch Freeze-Drying Process Using an Infrared Camera. *Eur. J. Pharm. Biopharm.* **2021**, *158*, 113−122.

(16) Harguindeguy, M.; Fissore, D. Micro Freeze-Dryer and Infrared-Based PAT: Novel Tools for Primary Drying Design Space Determination of Freeze-Drying Processes. *Pharm. Reserach* **2021**, *38*, 707−719.

(17) Colucci, D.; Maniaci, R.; Fissore, D. Monitoring of the Freezing Stage in a Freeze-Drying Process Using IR Thermography. *Int. J. Pharm.* **2019**, *566* (May), 488−499.

(18) Patel, S. M.; Bhugra, C.; Pikal, M. J. Reduced Pressure Ice Fog Technique for Controlled Ice Nucleation during Freeze-Drying. *AAPS PharmSciTech* **2009**, *10* (4), 1406−1411.

(19) Fang, R.; Bogner, R. H.; Nail, S. L.; Pikal, M. J. Stability of Freeze-Dried Protein Formulations: Contributions of Ice Nucleation Temperature and Residence Time in the Freeze-Concentrate. *J. Pharm. Sci.* **2020**, *109* (6), 1896−1904.

(20) Hottot, A.; Nakagawa, K.; Andrieu, J. Effect of Ultrasound-Controlled Nucleation on Structural and Morphological Properties of Freeze-Dried Mannitol Solutions. *Chem. Eng. Res. Des.* **2008**, *86* (2), 193−200.

(21) Petersen, A.; Rau, G.; Glasmacher, B. Reduction of Primary Freeze-Drying Time by Electric Field Induced Ice Nucleus Formation. *Heat Mass Transfer und Stoffueubertragung* **2006**, *42* (10), 929−938.

(22) Kramer, M.; Sennhenn, B.; Lee, G. Freeze-drying Using Vacuum-induced Surface Freezing. *J. Pharm. Sci.* **2002**, *91* (2), 433−443.

(23) Oddone, I.; Pisano, R.; Bullich, R.; Stewart, P. Vacuum-Induced Nucleation as a Method for Freeze-Drying Cycle Optimization. *Ind. Eng. Chem. Res.* **2014**, *53* (47), 18236−18244.

(24) Arsiccio, A.; Barresi, A. A.; De Beer, T.; Oddone, I.; Van Bockstal, P. J.; Pisano, R. Vacuum Induced Surface Freezing as an Effective Method for Improved Inter- and Intra-Vial Product Homogeneity. *Eur. J. Pharm. Biopharm.* **2018**, *128* (March), 210−219.

(25) Oddone, I.; Van Bockstal, P.-J.; De Beer, T.; Pisano, R. Impact of Vacuum-Induced Surface Freezing on Inter- and Intra-Vial Heterogeneity. *Eur. J. Pharm. Biopharm.* **2016**, *103*, 167−178.

(26) Oddone, I.; Barresi, A. A.; Pisano, R. Influence of Controlled Ice Nucleation on the Freeze-Drying of Pharmaceutical Products: The Secondary Drying Step. *Int. J. Pharm.* **2017**, *524* (1−2), 134−140.

(27) Pisano, R.; Capozzi, L. C. Prediction of Product Morphology of Lyophilized Drugs in the Case of Vacuum Induced Surface Freezing. *Chem. Eng. Res. Des.* **2017**, *125*, 119−129.

(28) Arsiccio, A.; Matejtschuk, P.; Ezeajughi, E.; Riches-Duit, A.; Bullen, A.; Malik, K.; Raut, S.; Pisano, R. Impact of Controlled Vacuum Induced Surface Freezing on the Freeze Drying of Human Plasma. *Int. J. Pharm.* **2020**, *582*, 119290.

(29) Pisano, R. Alternative Methods of Controlling Nucleation in Freeze Drying. In *Lyophilization of Pharmaceuticals and Biologicals: New Technologies and Approaches*; Methods in Pharmacology and Toxicology; Ward, K. R., Matejtschuk, P., Eds.; Springer Science: New York, NY, 2019; pp 79−111, DOI: 10.1007/978-1-4939-8928-7_4.

(30) Capozzi, L. C.; Pisano, R. Looking inside the 'Black Box': Freezing Engineering to Ensure the Quality of Freeze-Dried Biopharmaceuticals. *Eur. J. Pharm. Biopharm.* **2018**, *129*, 58−65.

(31) Patel, S. M.; Doen, T.; Pikal, M. J. Determination of End Point of Primary Drying in Freeze-Drying Process Control. *AAPS PharmSciTech* **2010**, *11* (1), 73−84.

(32) Pisano, R. Automatic Control of a Freeze-Drying Process: Detection of the End Point of Primary Drying. *Dry. Technol.* **2022**, *40*, 140−157.

(33) Van Bockstal, P.-J.; Corver, J.; De Meyer, L.; Vervaet, C.; De Beer, T. Thermal Imaging as a Noncontact Inline Process Analytical Tool for Product Temperature Monitoring during Continuous Freeze-Drying of Unit Doses. *Anal. Chem.* **2018**, *90* (22), 13591−13599.

(34) Capozzi, L. C.; Trout, B. L.; Pisano, R. From Batch to Continuous: Freeze-Drying of Suspended Vials for Pharmaceuticals in Unit-Doses. *Ind. Eng. Chem. Res.* **2019**, *58* (4), 1635−1649.

(35) Barresi, A.; Ghio, S.; Fissore, D.; Pisano, R. Freeze Drying of Pharmaceutical Excipients Close to Collapse Temperature: Influence of the Process Conditions on Process Time and Product Quality. *Dry. Technol.* **2009**, *27* (6), 805−816.

(36) Gonzalez, R. C.; Woods, R. E. *Digital Image Processing*, 2nd ed.; George, D. A., Ed.; Prentice Hall: Upper Saddle River, NJ, 2002.

(37) Canny, J. A Computational Approach to Edge Detection. *IEEE Trans. Pattern Anal. Mach. Intell.* **1986**, *PAMI-8* (6), 679−698.

(38) Prats-Montalbán, J. M.; de Juan, A.; Ferrer, A. Multivariate Image Analysis: A Review with Applications. *Chemom. Intell. Lab. Syst.* **2011**, *107* (1), 1−23.

(39) Harguindeguy, M.; Stratta, L.; Fissore, D.; Pisano, R. Investigation of the Freezing Phenomenon in Vials Using an Infrared Camera. *Pharmaceutics* **2021**, *13* (10), 1664.

(40) Nakagawa, K.; Hottot, A. Modeling of Freezing Step during Freeze-Drying of Drugs in Vials. *AIChE J.* **2007**, *53*, 1362−1372.

(41) Bosca, S.; Fissore, D.; Demichela, M. Risk-Based Design of a Freeze-Drying Cycle for Pharmaceuticals. *Ind. Eng. Chem. Res.* **2015**, *54* (51), 12928−12936.

(42) Bosca, S.; Barresi, A. A.; Fissore, D. On the Robustness of the Soft Sensors Used to Monitor a Vial Freeze-Drying Process. *Dry. Technol.* **2017**, *35* (9), 1085−1097.

(43) Lide, D. R. Properties of Ice and Supercooled Water. In *CRC Handbook of Chemistry and Physics*; Haynes, W. M., Ed.; CRC Press, Taylor & Francis Group: Boca Raton, FL, 2010; pp 6−12.

(44) Catté, M.; Dussap, C. G.; Achard, C.; Gros, J. B. Excess Properties and Solid-Liquid Equilibria for Aqueous Solutions of Sugars Using a UNIQUAC Model. *Fluid Phase Equilib.* **1994**, *96* (C), 33−50.

(45) Corti, H. R.; Angell, C. A.; Auffret, T.; Levine, H.; Buera, M. P.; Reid, D. S.; Roos, Y. H.; Slade, L. Empirical and Theoretical Models of Equilibrium and Non-Equilibrium Transition Temperatures of Supplemented Phase Diagrams in Aqueous Systems (IUPAC Technical Report). *Pure Appl. Chem.* **2010**, *82* (5), 1065−1097.

(46) Norrish, R. Equation for the Activity Coefficients and Equilibrium Relative Humidities. *JInternational J. Food Sci. Technol.* **1966**, *1*, 25−39.

(47) De Vito, F.; Veytsman, B.; Painter, P.; Kokini, J. L. Simulation of the Effect of Hydrogen Bonds on Water Activity of Glucose and Dextran Using the Veytsman Model. *Carbohydr. Polym.* **2015**, *117*, 236−246.

(48) Fissore, D.; Pisano, R. Computer-Aided Framework for the Design of Freeze-Drying Cycles: Optimization of the Operating Conditions of the Primary Drying Stage. *Processes* **2015**, *3* (2), 406−421.

(49) Shalaev, E.; Soper, A.; Zeitler, J. A.; Ohtake, S.; Roberts, C. J.; Pikal, M. J.; Wu, K.; Boldyreva, E. Freezing of Aqueous Solutions and Chemical Stability of Amorphous Pharmaceuticals: Water Clusters Hypothesis. *J. Pharm. Sci.* **2019**, *108* (1), 36−49.

(50) Chow, R.; Blindt, R.; Chivers, R.; Povey, M. A Study on the Primary and Secondary Nucleation of Ice by Power Ultrasound. *Ultrasonics* **2005**, *43* (4), 227−230.

(51) Kane, S. G.; Evans, T. W.; Brian, P. L. T.; Sarofim, A. F. Determination of the Kinetics of Secondary Nucleation in Batch Crystallizers. *AIChE J.* **1974**, *20* (5), 855−862.